

Multi-relation graph convolutional network for Alzheimer's disease diagnosis using structural MRI

Jin Zhang^a, Xiaohai He^{a,*}, Linbo Qing^a, Xiang Chen^b, Yan Liu^c, Honggang Chen^a

^a College of Electronics and Information Engineering, Sichuan University, Chengdu, Sichuan, 610065, China

^b Centre for Computational Imaging and Simulation Technologies in Biomedicine (CISTIB), School of Computing, University of Leeds, Leeds, UK

^c Department of Neurology, The Affiliated Hospital of Southwest Jiaotong University, The Third People's Hospital of Chengdu, Chengdu, Sichuan, 610031, China

ARTICLE INFO

Article history:

Received 24 August 2022

Received in revised form 30 March 2023

Accepted 4 April 2023

Available online 6 April 2023

Keywords:

Alzheimer's disease

Graph convolutional network

Structural magnetic resonance imaging

Deep learning

Medical image processing

ABSTRACT

Structural magnetic resonance imaging (sMRI) is widely applied in Alzheimer's disease (AD) diagnosis tasks by reflecting structural anomalies of the brain. Currently, most existing methods solely focus on pathological changes in disease-affected brain regions and ignore their potential associations and interactions, which provide valuable information for brain investigation. Meanwhile, how to construct effective structural brain graphs composed of nodes and edges remains appealing. To tackle these issues, in this paper, we propose a novel multi-relation reasoning network (MRN) to learn multi-relation-aware representations of brain regions in sMRI data for AD diagnosis, including spatial correlations and topological information. We frame distinguishing different disease statuses as the graph classification problem. Each scan is regarded as a graph, where nodes represent brain regions with abnormal changes selected by group-wise comparison, and edges denote semantic or spatial relations between them. Specifically, the dilated convolution module learns informative features to provide discriminative node representations for constructing brain graphs. Multi-type inter-region relations are then captured by the local reasoning module based on the graph convolutional network to provide a reliable basis for AD diagnosis, including geometric correlations and semantic interactions. Moreover, global reasoning is employed on the learned graph structure to achieve information aggregation and gradually generate the subject-level representation for AD diagnosis. We evaluate the effectiveness of our proposed method on the ADNI dataset, and extensive experiments demonstrate that our MRN achieves competitive performance for multiple AD-related classification tasks, compared to several state-of-the-art methods.

© 2023 Elsevier B.V. All rights reserved.

1. Introduction

Alzheimer's disease (AD) is a neurodegenerative and irreversible brain disorder, most prevalent in dementia [1]. Approximately 90 million people worldwide are diagnosed with AD, and the number of patients with AD is predicted to reach 300 million across the globe by 2050 [2,3]. AD begins with memory deficits and develops over disease, accompanied by issues in communication, orientation, and control of bodily functions. It is one of the leading causes of death in the elderly population [4,5]. To date, no curative treatment is available for AD, while some treatments such as medications, exercise, and memory training can ease symptoms or delay its deterioration [6]. Therefore, it is worthwhile to diagnose AD as accurately as possible, peculiarly in its early stage known as mild cognitive impairment (MCI),

which is the transition from cognitively normal (CN) to AD [7]. The diagnosis of AD is essential because it helps delay disease progression and improves the general well-being of patients [8].

In recent decades, brain imaging technologies have been increasingly investigated to discover relevant biomarkers in the human brain for AD diagnosis [9–14]. Structural magnetic resonance imaging (sMRI) is a non-invasive imaging technology that can produce detailed three-dimensional (3D) anatomical images of the brain and model anatomical brain changes affected by AD [15–17]. sMRI plays a crucial role in clinical diagnosis and AD studies. With high contrast of soft tissues and excellent spatial resolution, sMRI scans can visualize details and subtle changes in brain tissues, aiding in AD diagnosis. Based on sMRI scans, various computer-aided diagnosis methods are proposed for the early detection of AD and MCI.

Recently, deep learning methods shows remarkable success in computer vision tasks such as medical imaging classification. In particular, deep convolutional neural networks (CNNs) are empirically verified to have the excellent ability to learn high-level

* Corresponding author.

E-mail address: hxh@scu.edu.cn (X. He).

features from sMRI data and significantly boost the performance of AD diagnosis with the efforts of many researchers [18–21]. For example, Liu et al. [22] proposed a 3D deep convolutional neural network (CNN) for AD diagnosis and found that increasing the width of the model produced significant gains. Spasov et al. [23] used 3D separable and grouped convolutions for extracting high-level representations from full-volume sMRI data for AD diagnosis. Most existing deep learning methods using full-volume MRI scans for AD diagnosis are so complicated that they require considerable computational resources and time during training. Models are not the more complex the better, so it is important to improve diagnostic accuracy using relatively simple methods with efficient networks. The deep-learning-based AD diagnosis methods that achieve competitive results mainly include two steps: extracting features from local image regions and then combining the extracted features for further classification. Lian et al. [24], for instance, proposed to automatically identify discriminative local patches in the whole sMRI data, upon which multi-scale feature representations were then fused for AD diagnosis. Zhu et al. [25] designed a multi-instance deep learning model to identify discriminative pathological locations and learn discriminative structural features from local sMRI regions for AD diagnosis. However, most existing methods generally focus on extracting image features of disease-related brain regions, disregarding location information and potential interactions between brain regions. The spatial location relationship and topological structure of discriminative brain regions in sMRI scans belonging to different disease states are different. Therefore, using spatial correlations and topological information between brain regions and combining their local texture information is crucial for AD diagnosis, understanding disease-affected imaging biomarkers, and pathogenesis exploration. In particular, it is still challenging to construct flexible and effective brain structural connectivity graphs that reflect complementary spatial correlations and topological information of disease-related regions in sMRI scans for AD diagnosis. Moreover, since brain atrophy typically occurs in localized regions, only a few regions in sMRI scans have obvious structural changes that are highly associated with pathological features, while the rest of the regions provide little relevant information for AD diagnosis. Therefore, the primary challenge of deep-learning-based methods based on sMRI scans for AD diagnosis is to locate important brain regions in sMRI scans that are significantly affected by AD/MCI and enhance discriminative features within those local regions.

To tackle the issues addressed above, we propose an end-to-end multi-relation reasoning network (MRN) for AD diagnosis using sMRI data, which is relatively simple and effective. First, the group-wise comparison is performed on sMRI scans to obtain key disease-related brain regions and discover imaging biomarkers, based on which multi-relation brain structural connectivity graphs are constructed, including a semantic graph with dynamic edges and a bidirectional spatial graph. Then, the local reasoning (LR) module including the semantic and spatial relation encoders is exploited to learn the spatial relations and potential interactions between regions distributed in the brain for AD diagnosis taking advantage of GCN. Finally, a graph-level representation of the disease state classification is generated by doing global reasoning. The classification tasks include AD vs. CN (differentiating AD from CN), MCI vs. CN (differentiating MCI from CN) and AD vs. MCI vs. CN (distinguishing between AD, MCI and CN). Potential applications of MRN include AD auxiliary diagnosis, which can help doctors assess conditions more efficiently and quickly, and improve diagnostic accuracy. The main contributions of our study are summarized as follows.

1. We propose a novel network named multi-relation reasoning network (MRN) that models AD diagnosis tasks as a graph classification problem to improve the performance of sMRI-based AD diagnosis, which assists diagnosticians to explore potential imaging biomarkers.
2. Brain connectivity graphs are constructed based on the disease-related brain regions selected by group-wise comparisons to represent sMRI data, containing a semantic graph with dynamic edges and a bidirectional labeled spatial graph.
3. To the best of our knowledge, this is the first study to learn multi-relation-aware representations of discriminative brain regions in sMRI data for AD diagnosis, which captures spatial correlations and potential interactions between them using GCN to provide valuable information for AD diagnosis.
4. We evaluate the effectiveness of the proposed method in the public dataset ADNI, and the experimental results demonstrate that MRN achieves promising performance for multiple AD-related classification tasks. We further investigate the influence of the left and right brain regions on the performance of AD diagnosis, implying that left regions have more obvious disease-induced structural changes than the right regions.

The remaining of this study is organized as below: Section 2 introduces the related works. Section 3 describes the material used for evaluation and the proposed method in detail. Section 4 reports the experimental settings, evaluation criteria and experimental results. Section 5 presents the discussions of this work. Finally, the conclusion is outlined in Section 6.

2. Related work

In this section, we briefly introduce previous work on computer-aided AD diagnosis based on sMRI scans. According to the feature representation used for classification, the previous AD diagnosis studies could be categorized into two groups, including the machine-learning-based and deep-learning-based methods.

2.1. Machine-learning-based methods

The machine-learning-based methods are usually comprised of two primary steps: extracting quantitative features from sMRI data and then applying traditional machine-learning classifiers. Feature extraction is a critical component of machine-learning-based methods. Features with high discrimination ability can train the classifier quickly and distinguish different classes effectively. These hand-crafted features include measures of brain volume, cortical thickness, white matter integrity, or other structural features. Hett et al. [26], for instance, proposed a novel texture-based grading method that studies the potential of multi-directional texture maps extracted with 3D Gabor filters to improve the performance of AD diagnosis. Plochanski et al. [27] performed the classification of AD and CN based on the sulcal surface features extracted by computing a medial surface from sulcal meshes. Kloppel et al. [28] used gray matter (GM) density maps extracted from the whole brain as input to a linear support vector machine (SVM) classifier to achieve AD diagnosis. Furthermore, since volumetric sMRI scans contain millions of voxels, these methods are often developed using feature selection/reduction algorithms. Wang et al. [29] and Sørensen et al. [30] proposed to use of the hippocampal features in sMRI scans to assist in AD diagnosis, as the hippocampus is known to be particularly affected by the AD pathological process. Additionally, several studies explored combining complementary information from

the hippocampus and other brain regions in sMRI scans for AD diagnosis. For instance, Ahmed et al. [31] fused features extracted from the hippocampus and posterior cingulate cortex to train SVM classifiers for AD/MCI diagnosis.

Machine learning-based methods for AD diagnosis often use hand-crafted features such as GM density maps, cortical thickness, or hippocampal shape measurements to construct classifiers. However, using independently-extracted features and subsequent classifiers may lead to sub-optimal diagnostic performance due to potential heterogeneities between them.

2.2. Deep-learning-based methods

Lately, deep learning has made remarkable achievements in computer vision, which supplies various ideas for diagnosing AD. Using CNNs or other deep learning architectures can learn the features of different dimensions from the sMRI data and reduce the complexity of manual feature extraction. Better features obtained from sMRI scans can contribute to the accurate AD diagnosis by capturing complex and nonlinear relationships between features and the disease state. In general, deep-learning-based methods for AD diagnosis can be categorized into four groups according to the input type: (1) 2D slice-level [32–34], (2) 3D patch-level [24,35–37], (3) region-of-interest (ROI) level [38–40] and (4) 3D subject-level [23,41,42].

2D slice-level: This kind of method utilizes a 2D CNN with a set of 2D slices obtained from 3D sMRI scans as the input [43]. Valliani et al. [32] used a pre-trained CNN to extract cross-domain features that enhanced the low-level interpretation of images and achieved significant improvements in the accuracy of AD diagnosis. Rashid et al. [34] presented a framework called BicephNet, which modeled the intra- and inter-slice information of 2D sMRI slices to diagnose AD and had an interpretation functionality to understand the classification decision. These algorithms are highly dependent on the selection methods of the input 2D slices, which may lead to loss of inter-slice information and data leakage.

3D patch-level: Methods belonging to this group typically divide an sMRI scan into a set of 3D patches as input. By automatically locating informative patches in sMRI scans, Lian et al. [24] designed a hierarchical fully convolutional network for joint learning and fusing feature representations from patches, regions, and subjects for AD diagnosis. Qiu et al. [37] developed a framework for selecting high-risk patches from disease probability maps, upon which the accuracy of AD diagnosis can be improved. The main advantages of these methodologies are lower memory costs and fewer parameters to learn.

ROI-level: The inputs for this type of approach are ROIs partitioned from brain sMRI scans. Considering the extracted disease-related ROI as an instance, Liu et al. [38] constructed a bag with multiple instances to represent each subject and proposed a multi-instance learning network for AD classification. Liu et al. [8] developed a multi-task method based on a CNN to jointly distinguish AD and segment hippocampus, which is well-known to be one of the most important regions in AD among all brain ROIs. A significant advantage of ROI-level methods is that the inputs are small, which reduces the risk of overfitting. Moreover, with the development of graph convolutional networks (GCN), some researchers have employed them in sMRI data to learn structural representations of the brain for disease classification [44–46]. Zhu et al. [45] designed a personalized network for AD diagnosis via coupling interpretable feature learning with dynamic graph learning into GCN to produce a reliable diagnosis. Zhou et al. [46] proposed a GCN framework using multi-modal brain imaging data, which enhances the performance of AD diagnosis and identifies biomarkers associated with the disease. Most of

the existing GCN-based AD diagnosis methods using sMRI scans involve only one graph and cannot completely learn the topology information.

3D subject-level: AD diagnosis is employed at the subject level using full-volume MRI scans. Jin et al. [47] introduced an attention mechanism into a 3D ResNet architecture to improve the diagnosis performance and further explore potential brain regions related to the disease. Liu et al. [22] reported that extending the model width and incorporating age information can boost the performance of a 3D CNN in distinguishing AD using brain sMRI scans. The drawback of this methodology is that compared with the number of network parameters updated during the training process, the number of sMRI scans is small, thus increasing the risk of overfitting.

Several deep-learning-based studies using sMRI data for AD diagnosis have attempted to extract rich information to provide more accurate classification results. Despite achieving great overall performance, most of the above methods ignore the spatial correlations and topological information between brain regions, which is crucial for AD diagnosis and understanding the interactions between disease-affected brain regions. Moreover, not all brain regions are equally affected by AD/MCI, which poses a challenge in identifying the regions that are significantly related to the disease and avoiding the interference of redundant information. This is an important concern in AD diagnostic research. Therefore, highlighting the discriminative features while retaining the potential correlations among brain regions is still a challenge in the AD diagnosis task.

3. Materials and method

3.1. Dataset

3.1.1. Data acquisition

This paper uses T1-weighted sMRI data from the Alzheimer's Disease Neuroimaging Initiative (ADNI) [48] dataset, the largest publicly available dataset for studying neuroimaging-based AD diagnosis. A total of 3492 1.5T/3T T1-weighted sMRI scans from 459 CN subjects, 768 MCI subjects and 417 AD subjects from the ADNI-1, ADNI-GO and ADNI-2 phases constitute the experimental dataset. These scans have been preprocessed with specific image preprocessing steps including multiplanar reconstruction (MPR), Gradwarp, B1 non-uniformity correction, and N3 intensity normalization. The collected sMRI scans are divided into three categories: AD, MCI, and CN. As subjects are screened at multiple time points for follow-up visits, each subject has at least one scan, which means that the scans from one subject have a unique subject ID and a different session ID. To prevent data leakage [7], the scans are randomly split by subject ID into training, validation and testing sets following [22,34,49], with a ratio of 8:1:1. Their details are presented in Table 1. With this data partitioning approach, all available scans from one subject are allocated to the training, validation, or testing sets, without data from one subject splitting across the three sets. The model with the highest validation accuracy is saved to obtain the final performance on the testing set. The data is split before preprocessing to prevent data leakage mentioned in AD diagnosis studies [7]. Data leakage due to scans of the same subject appearing in the training and testing sets has been demonstrated to artificially improve diagnosis performance [18,50]. Clinical criteria including the Mini-Mental State Examination (MMSE), global clinical dementia rating (CDR), and clinical dementia rating scale sum of boxes (CDR-SOB) scores and demographic information are mainly considered for balanced data partitioning with similar distributions of scales between the training, validation and testing sets. The demographic information and clinical scale scores of the studied scans are reported in terms of mean (standard deviation) in Table 1.

Table 1
Summary of demographics and clinical scale scores of the dataset.

Split	Diagnosis	Subjects	Scans	Age	MMSE	CDR	CDR-SOB
Training	CN	360	837	76.22(6.21)	28.95(1.88)	0.02(0.17)	0.10(0.34)
	MCI	613	1350	74.81(7.82)	27.34(2.75)	0.48(0.16)	1.64(1.10)
	AD	345	586	75.86(7.33)	21.59(4.65)	0.91(0.49)	5.45(2.74)
Validation	CN	50	121	75.82(5.90)	29.14(1.09)	0.02(0.14)	0.11(0.30)
	MCI	72	185	75.57(7.41)	27.34(2.28)	0.49(0.11)	1.67(1.10)
	AD	36	54	73.82(7.48)	22.02(3.67)	0.90(0.39)	5.53(2.35)
Testing	CN	49	121	75.44(6.02)	29.09(1.18)	0.03(0.17)	0.11(0.33)
	MCI	79	184	73.79(7.40)	27.42(2.82)	0.47(0.19)	1.61(1.02)
	AD	36	54	74.60(8.38)	22.06(4.04)	0.83(0.38)	5.21(2.64)

Table 2
Details of the 12 most important regions in the AAL3 atlas.

Rank	Region ID	Region name	Region abbreviation	Kendall correlation
1, 3	41, 42	Left and Right Hippocampus	IHIP and rHIP	-0.3304, -0.3172
2, 4	45, 46	Left and Right Amygdala	IAMYG and rAMYG	-0.3207, -0.3005
5, 6	43, 44	Left and Right ParaHippocampal gyrus	IPHG and rPHG	-0.2820, -0.2693
9, 8	89, 90	Left and Right Middle temporal gyrus	IMTG and rMTG	-0.2295, -0.2343
7, 10	93, 94	Left and Right Inferior temporal gyrus	IITG and rITG	-0.2423, -0.2180
12, 11	91, 92	Left and Right Temporal pole: middle temporal gyrus	ITPOmid and rTPOmid	-0.2127, -0.2155

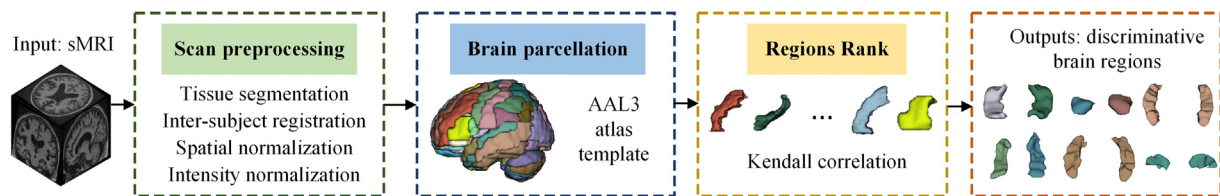


Fig. 1. The illustration of the data preprocessing. The input of the data preprocessing process is an sMRI scan, and the outputs are discriminative brain regions significantly associated with AD/MCI through scan preprocessing, brain parcellation and regions rank.

3.1.2. Data preprocessing

For this study, sMRI scans are preprocessed using the Clinica software platform¹ [51], which supports FSL,² SPM³ and FreeSurfer [52]. The input is the sMRI scans transformed to the Brain Imaging Data Structure (BIDS) format. First, tissue segmentation, such as gray matter, white matter and cerebrospinal fluid, inter-subject registration using Dartel, and spatial normalization into standard Montreal Neurological Institute (MNI) space are performed on the input images. Moreover, the intensity normalization is done by the min-max normalization. After intensity normalization, brain parcellation is performed with the well-known atlas Automated Anatomical Labeling 3 (AAL3) [53] with manually-labeled anatomical regions. The idea builds on spatial normalization, which ensures that the same brain region appears in the same location across different scans. The atlas AAL3 can therefore be used as a mask to parcellate the brain. Finally, a set of 166 anatomical regions are obtained by atlas warping and the average gray-matter density is calculated in each brain region. The illustration of data preprocessing is shown in Fig. 1.

Structural changes in some brain structures are strongly correlated with the disease [15]; therefore, we rank the importance of informative regions by group-wise comparisons according to local morphological features to identify brain regions that have significant group differences. Kendall correlation analysis [54] is performed on the gray matter density of each brain region (X) and disease category (Y) to measure the correlation, strength of association and direction of the relationship between them as

follows:

$$k = \frac{C - D}{\sqrt{(T - T_x)(T - T_y)}} \tag{1}$$

where k is the Kendall correlation coefficient. C is the number of concordant pairs and D is the number of discordant pairs. (x_1, y_1) and (x_2, y_2) are concordant if $(x_1 - x_2)(y_1 - y_2) > 0$ and discordant if $(x_1 - x_2)(y_1 - y_2) < 0$. $T = n(n - 1)/2$, is the total number of pairwise comparisons, where n is the sample size. $T_x = \sum_x t_x(t_x - 1)/2$, $T_y = \sum_y t_y(t_y - 1)/2$, where t_x is the number of identical y in the gray matter density (X), t_y is the number of identical x in the disease state (Y).

Statistical analysis is performed using the SPSS 26. Regional differences are examined in the gray matters between the three categories, which are expressed by the absolute value of the Kendall correlation coefficient. A larger absolute value indicates that the region is closely correlated with the disease status; that is, the region is more discriminative. The direction of the relationship is indicated by the sign of the coefficient, and a - sign means a negative correlation between X and Y . The top 12 high-ranked regions with statistically significant differences between groups are selected for experiments and analysis, including the bilateral hippocampus, bilateral amygdala, bilateral parahippocampal gyrus and bilateral temporal gyrus, as shown in Fig. 2. Their details are presented in Table 2. These regions are consistent with some medical research [25,55], which predominate the histopathological changes in the clinical manifestations of AD.

3.2. Overview of the proposed framework

As the human brain is a topologically complex network, we regard sMRI-based AD diagnosis as a graph classification problem. Compared with CN subjects, the potential associations and

¹ <http://www.clinica.run>.
² <https://fsl.fmrib.ox.ac.uk/fsl>.
³ <https://www.fil.ion.ucl.ac.uk/spm>.

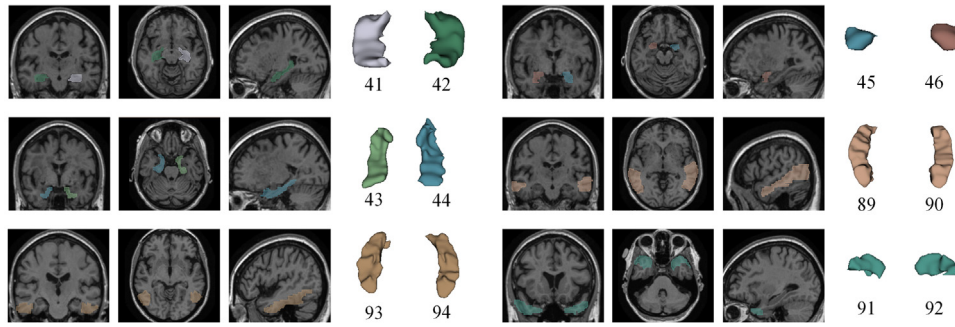


Fig. 2. Representation of the top-12 disease-affected brain regions.

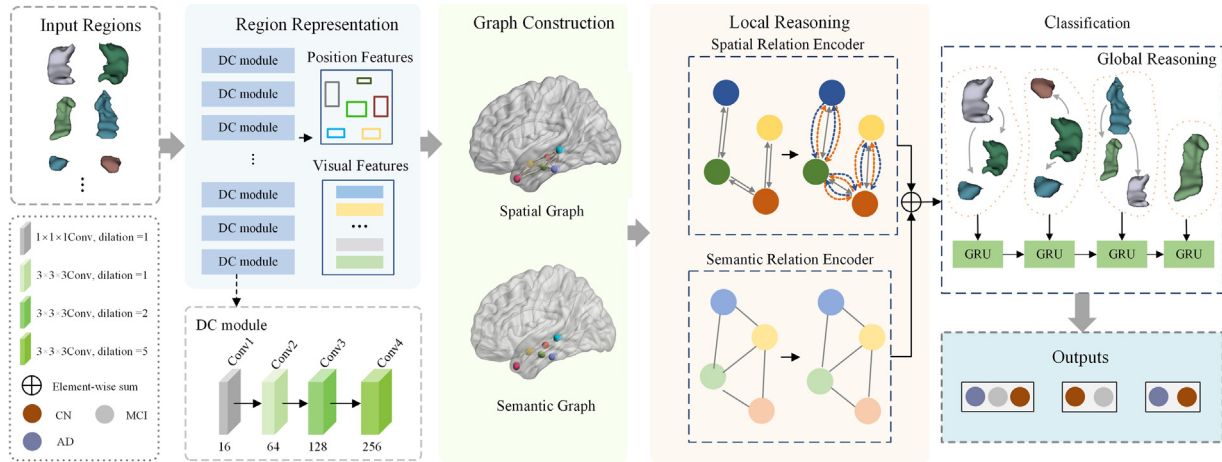


Fig. 3. Overview of the proposed multi-relation reasoning network (MRN), which includes four components: (1) region representation module, (2) graph construction module, (3) local reasoning module, and (4) classification module.

interactions between the discriminant brain regions in the sMRI data are different in patients with AD and MCI. Therefore, we develop a novel multi-relation reasoning network (MRN) to capture spatial correlations and potential interactions between brain regions associated with disease, providing reliable information for AD diagnosis. As shown in Fig. 3, our proposed method mainly consists of four components: region representation learning via dilated convolution (Section 3.3), construction of brain connectivity graphs (Section 3.4), extraction of spatial interactions and topological information (Section 3.5), and information aggregation through global reasoning for classification (Section 3.6). Since abnormal brain atrophy occurs in few local regions, especially at the MCI stage, selected brain regions in data preprocessing are used as inputs. Three classifications (AD vs. CN, MCI vs. CN and AD vs. MCI vs. CN) are considered as AD-related diagnosis tasks in this paper. For these three classification tasks, the inputs of the framework are respectively six, eight and twelve paired discriminative brain regions that are determined experimentally, and the outputs are predictions of the disease status.

3.3. Region representation

Since AD is believed to affect various brain regions differently, using full-volume sMRI data for AD diagnosis may provide irrelevant information, which leads to a reduction in diagnostic performance. Therefore, the top- K regions with the highest correlation values are selected as inputs. Considering that the sizes of the input regions are different and relatively small, the dilated convolution module is designed to learn more informative representations of discriminative regions, including near and distant information. The proposed dilated convolution (DC) module

includes four blocks, each consisting of 3D dilated convolution, instance normalization (IN) and ReLU layers. First, the input region is passed through a convolution layer with a $1 \times 1 \times 1$ convolution filter and a stride of 1, which can be considered as a linear transformation of input channels. The followed dilated convolution layers severally contain 64, 128 and 256 filters with a small kernel size of $3 \times 3 \times 3$, and the dilated coefficients are set to 1, 2 and 5, respectively. Instead of using large convolution filters, we utilize dilations in the convolution layers to detect more relevant information by increasing the receptive fields without additional computational overhead. Finally, the global average pooling operation is performed to generate the region features. Given an sMRI scan, the informative brain regions are cropped and fed into the DC module to produce region representations $\mathcal{V} = \{v_i\}_{i=1}^K$ with K regions (v_i denotes the 256-dimensional feature of each brain region).

3.4. Graph construction

3.4.1. Semantic graph

Taking advantage of the DC module, each sMRI scan can be represented by a set of features $\mathcal{V} = \{v_i\}_{i=1}^K$, such that each feature v_i encodes a brain region. Upon this, a fully connected graph $\mathcal{G}_{sem} = (\mathcal{V}, \mathcal{E}_{sem})$ is constructed, where \mathcal{V} and \mathcal{E}_{sem} are the sets of nodes and edges, respectively. Each brain region is treated as a node with representation v_i . The edge set \mathcal{E}_{sem} is described as the correlation of brain regions, which is estimated dynamically from the region representations as Eq. (2) during training instead of being pre-defined and shared for all sMRI scans. The semantic graph \mathcal{G}_{sem} is specific for each sMRI scan

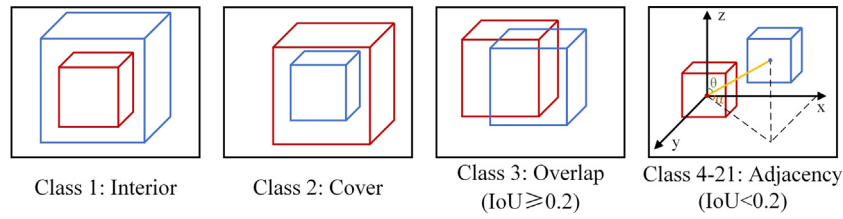


Fig. 4. Definition of twenty-one kinds of spatial relations between two brain regions i and j . The red cube represents region i and the blue cube indicates region j .

which captures content-related region dependencies.

$$\mathcal{E}_{sem} = \delta(W_r \mathcal{V}) \quad (2)$$

where $\delta(\cdot)$ is the sigmoid activation function and W_r is the weight to formulate the dynamic correlations \mathcal{E}_{sem} .

3.4.2. Spatial graph

Especially, spatial information contributes to the understanding of potential biomarkers for AD diagnosis, which reflects the space appearance of individual regions and the geometric relations between regions. Therefore, a bidirectional spatial graph is built to fully exploit relative spatial relations between crucial brain regions. Given two brain regions i and j , their locations are expressed as (x_i, y_i, z_i) and (x_j, y_j, z_j) , which are the normalized coordinates of the center of mass. The edges and corresponding labels between them depend on the Intersection over Union (IoU), relative distance d_{ij} ($d_{ij} = \sqrt{(x_j - x_i)^2 + (y_j - y_i)^2 + (z_j - z_i)^2}$), relative polar angle θ_{ij} and relative azimuthal angle α_{ij} between regions i and j in the spherical coordinate system. There are 21 types of position relations as illustrated in Fig. 4. Two special situations are firstly discussed for joining edges from region i to region j with its geometric relation label as ‘interior’ and ‘cover’, where ‘interior’ stands for that region i is fully contained in region j (type 1), while ‘cover’ represents that region i completely covers region j (type 2). Otherwise, if the IoU is greater than 0.2, an edge is directly established, which is defined as ‘overlap’ (type 3). Furthermore, when the ratio φ_{ij} of the relative distance d_{ij} to the diagonal length of full-volume sMRI scan is less than 0.5, the edge is defined according to θ_{ij} and α_{ij} , and the spatial relation ‘adjacency’ is marked as $6 * \lfloor \frac{\theta_{ij}}{60^\circ} \rfloor + \lfloor \frac{\alpha_{ij}}{60^\circ} \rfloor + 4$ (type 4–21). When the ratio $\varphi_{ij} > 0.5$ and $\text{IoU} < 0.2$, the spatial correlation between region i and region j is too weak to establish an edge. It is worth noting that the spatial graph $\mathcal{G}_{spa} = (\mathcal{V}, \mathcal{E}_{spa})$ is directional, where edges $\varepsilon_{i,j}$ and $\varepsilon_{j,i}$ are symmetric.

3.5. Multi-relation reasoning on graphs

After graph construction, each sMRI scan is represented by two graphs \mathcal{G}_{sem} and \mathcal{G}_{spa} . The local reasoning (LR) module is developed to contextually encode brain regions with semantic and spatial graph structures into multi-relation-aware representations. This module involves two encoders: semantic relation encoder and spatial relation encoder.

3.5.1. Semantic relation encoder

To enrich the region-level representations for AD diagnosis, a semantic relation encoder via GCN [56] is introduced to derive the semantic relation perception on the dynamic graph between brain regions in an adaptive manner. GCN inductively updates the node representation by aggregating the features of adjacent nodes. In the semantic relation encoder, the correlation matrix \mathcal{E}_{sem} is calculated adaptively by relying on input representations, which is different from the traditional GCN in that its adjacency matrix is fixed and shared with all sMRI scans. Since every sMRI

scan has a personalized \mathcal{E}_{sem} , it promotes the representative ability of the semantic relation encoder and reduces the possibility of over-fitting caused by static graphs. The representations with semantic relations $V^1 = \{v_1^1, v_2^1, \dots, v_k^1\}$ are updated as follows:

$$V^1 = f(\mathcal{E}_{sem} \mathcal{V} W_1) \quad (3)$$

where $f(\cdot)$ is the LeakyReLU function, \mathcal{E}_{sem} is the dynamic correlation matrix, and W_1 is the state-update weights, \mathcal{V} denotes the node features.

3.5.2. Spatial relation encoder

Because the spatial graph is directional and contains labels indicating spatial relations, different directions and labels between any two nodes need to be updated using separate transformation matrices and biases, respectively. To address this, taking advantage of the GCN and attention mechanism, a spatial encoder is employed to perform reasoning on the spatial graph so that it is sensitive to aggregate information directionally and focus on potentially important edges automatically. Therefore, the representation of a region i in the spatial graph is formulated as follows:

$$v_i^2 = \sigma \left(\sum_{j \in N(v_i)} W_{dir(i,j)} \cdot (\alpha_{ij} v_j) \right) \quad (4)$$

where W is the projection matrix and $\sigma(\cdot)$ denotes a nonlinear function. $N(v_i)$ indicates the neighbor set of v_i , including v_i itself. α_{ij} is the attention coefficient, and the calculation formula is as follows:

$$\alpha_{ij} = \frac{\exp \left((W_\varphi v_i^1)^T \cdot V_{dir(i,j)} v_j + b_{lab(i,j)} \right)}{\sum_{j \in N(v_i)} \exp \left((W_\varphi v_i^1)^T \cdot V_{dir(i,j)} v_j + b_{lab(i,j)} \right)} \quad (5)$$

where W_φ denotes the transformation matrix and $dir(i, j)$ represents the direction of edges $(v_i - v_j, v_j - v_i)$. $lab(i, j)$ and $lab(j, i)$ are labels from v_i to v_j and v_j to v_i , respectively.

To enrich the ability of the model, multi-head attention [57] is utilized, which concatenates the output features from each attention head to obtain the region-level representations with spatial correlation perception $V^2 = \{v_1^2, v_2^2, \dots, v_k^2\}$ as follows:

$$v_i^2 = \parallel_{m=1}^M \sigma \left(\sum_{j \in N(v_i)} W_{dir(i,j)}^m \cdot (\alpha_{ij}^m v_j) \right) \quad (6)$$

where M represents the number of independent attention mechanisms.

3.6. Classification

The final region-level representation V^* is obtained by adding the semantic-relation aware representation V^1 and the spatial-relation aware representation V^2 as $V^* = V^1 + V^2$ to enhance classification accuracy. Then, inspired by [58], the sequence of

brain region features $V^* = \{v_1^*, v_2^*, \dots, v_k^*\}$ is fed one by one into gated recurrent unit (GRU) [59] for global reasoning to select the discriminative information and filter out the unimportant one to generate the subject-level representation. During this process, the subject-level representation gradually grows and is updated in the memory cell (hidden state).

At each reasoning step t , the update gate z_t analyzes the current input region feature v_t^* and the description of the whole scan at the last step m_{t-1} to decide how much the past information passes. z_t is computed by:

$$z_t = \text{sigmoid}(W^z v_t^* + U^z m_{t-1} + b_z) \quad (7)$$

where W^z , U^z and b_z are weights and bias.

The newly added memory content helping grow the subject-level representation is computed as follows:

$$\tilde{m}_t = \tanh(W^m v_t^* + U^m (r_t \circ m_{t-1}) + b_m) \quad (8)$$

where W^m , U^m and b_m are weights and bias. \circ represents an element-wise multiplication. r_t denotes the reset gate that computes similarly to the update gate. r_t decides what information to forget based on the reasoning between v_t^* and m_{t-1} , which is calculated as follows:

$$r_t = \text{sigmoid}(W^r v_t^* + U^r m_{t-1} + b_r) \quad (9)$$

where W^r , U^r and b_r are weights and bias.

Then subject-level representation m_t at the current step is a linear interpolation utilizing update gate z_t between the previous representation m_{t-1} and the new content \tilde{m}_t as follows:

$$m_t = (1 - z_t) \circ m_{t-1} + z_t \circ \tilde{m}_t \quad (10)$$

Each brain region feature v_t^* contains global relation information, so the update of m_t is based on reasoning on a graph topology, which considers both the current local region and global correlations. The memory cell m_k at the end of the sequence V^* is defined as the final subject-level representation V , where k is the length of V^* .

For classification, two fully connected layers and activation function $\text{softmax}(\cdot)$ are stacked with the subject-level representation V as input, which predicts the probability score of the input sMRI belonging to a specific category. The loss function for AD diagnosis is the cross-entropy loss between the predicted label and the ground truth label.

4. Results

4.1. Experimental settings

All experiments are conducted using Python 3.6 based on the Pytorch library. The proposed framework is implemented using a computer with Ubuntu 18.04 operating system, which contains an NVIDIA GeForce GTX 3090 GPU (24 GB). Training is performed using the Adam [60] optimizer with a batch size of 16 within 200 epochs. The initial learning rate is 0.0001, which is then adjusted according to the cosine annealing strategy.

4.2. Evaluation criteria

To quantitatively evaluate the results of AD diagnosis, five commonly-used metrics [61–63], including the overall accuracy (ACC), sensitivity (SEN), specificity (SPE), F1-score (F1) and the area under the receiver operating characteristic curve (AUC) are utilized as evaluation criteria, which are defined as follows:

$$\text{ACC} = \frac{\sum_{i=1}^{N_c} TP_i}{N} \quad (11)$$

$$\text{SEN} = \frac{\sum_{i=1}^{N_c} \frac{TP_i}{TP_i + FN_i}}{N_c}, \text{SPE} = \frac{\sum_{i=1}^{N_c} \frac{TN_i}{FP_i + TN_i}}{N_c} \quad (12)$$

$$\text{F1} = \frac{\sum_{i=1}^{N_c} \frac{2 \times TP_i}{2 \times TP_i + FN_i + FP_i}}{N_c} \quad (13)$$

where TP_i , FP_i , FN_i , TN_i denote the true positive, false positive, false negative and true negative for the i th disease status, and N_c is the number of total classes. N is the number of total samples in N_c classes. N_c equals 2 and 3 in the two-class and multi-class diagnosis tasks, respectively.

4.3. Experimental results

4.3.1. Comparison with other methods

To justify the performance of the MRN, we compare it with state-of-the-art (SOTA) sMRI-based AD diagnosis approaches and baseline methods on the same experimental data in three classification tasks (AD vs. CN, MCI vs. CN, and AD vs. MCI vs. CN).

AD vs. CN: This classification task is considered to be the simplest in AD-related diagnosis because the sMRI scans of AD patients show highly obvious changes, that is, a significant degree and range of brain atrophy, compared with healthy groups. This facilitates the deep learning network to learn the differences between the two statuses from the sMRI images. It is important to stress that the results labeled * from comparative methods [8, 37, 40, 47] are not completely comparable, since the sMRI scans and preprocessing progress adopted in these studies are not identical, it is not known whether data leakage occurred, the comparisons are made for reference only. Three classical networks for solving classification problems, 3D ResNet-18, ResNet-50 and ResNet-101 [64], and Extended-2D [65], Biceph-Net [34], and CDFA [22] are further utilized for AD classification using full-volume sMRI data same as in this study, for a fair comparison.

Several observations are summarized in Table 3. First, the diagnostic performance reduces as the depth of the ResNet increased, indicating that increasing the depth does not always lead to better accuracy in AD diagnosis. A possible explanation for the finding is that increasing the depth increases the number of parameters to be trained, leading to a higher possibility of overfitting. Second, our MRN achieves a highly competitive performance, with ACC reaching 92.57%, which is higher than that of the SOTA methods. Furthermore, compared with subject-level methods using the same data and preprocessing process, our method yields a significant improvement in the overall performance, corresponding to a 1.71% increase over CDFA [22] (90.86%). This result might be explained by the fact that the proposed MRN can extract the topological and spatial correlations of local region-level brain structures through GCN better than the full-volume brain features. The performance comparison validates the effectiveness of regrading sMRI brain regions as graphs for AD vs. CN diagnosis.

MCI vs. CN: We further compare MRN with competing methods for more complex MCI vs. CN classification task. This is considered much more challenging than the AD vs. CN classification because sMRI scans from patients with MCI show no obvious disease-induced structural changes visually. Therefore, it is difficult to use traditional CNN to implement the MCI vs. CN classification, as they may overlook subtle changes in sMRI scans, leading to misclassification.

It can be seen from Table 4 that MRN achieves better performance in the MCI vs. CN diagnosis task in most cases. For example, the AUC (73.14%) and F1 (80.39%) yielded by the proposed framework are better than those obtained using the other

Table 3
Performance comparison with SOTA methods for AD vs. CN classification.

Method	Subjects	AD vs. CN classification (%)				
		ACC	SEN	SPE	AUC	F1
ACN [47] ^a	227AD + 305CN	92.10	89.00	94.40	94.10	–
IDLF [37] ^a	188AD + 229CN	83.40	76.70	88.90	–	80.60
ADDL [7] ^a	336AD + 330CN	89.00	–	–	–	–
JHSAC [8] ^a	97AD + 119CN	88.90	86.60	90.80	92.50	–
BSN [40] ^a	65AD + 65CN	85.30	–	–	–	–
TLCF [66] ^a	209AD + 302CN	89.24	85.58	91.72	95.00	–
Extended-2D [65]	345AD + 360CN	74.65	43.90	88.37	75.79	51.66
Biceph-Net [34]	345AD + 360CN	83.43	79.63	85.12	82.38	74.78
CDFA [22]	345AD + 360CN	90.86	92.59	90.08	95.73	86.21
ResNet-18	345AD + 360CN	89.14	81.48	92.56	93.07	82.24
ResNet-50	345AD + 360CN	88.57	87.04	89.26	93.43	82.46
ResNet-101	345AD + 360CN	88.57	87.04	89.26	95.24	82.46
MRN	345AD + 360CN	92.57	83.33	96.69	97.64	87.38

^aMeans just as a reference since the selected experimental data and data preprocessing processes in these methods are different.

Table 4
Performance comparison with SOTA methods for MCI vs. CN classification. The best performances using the same data and different data are shown in bold and underlined, respectively.

Method	Subjects	MCI vs. CN classification (%)				
		ACC	SEN	SPE	AUC	F1
AIN [67] ^a	251MCI + 302CN	69.44	–	–	76.00	66.00
JHSAC [8] ^a	233MCI + 119CN	76.20	<u>79.50</u>	69.80	77.50	–
BSN [40] ^a	65MCI + 65CN	83.70	–	–	–	–
TLCF [66] ^a	251MCI + 302CN	75.58	72.94	<u>77.81</u>	83.00	<u>73.00</u>
Extended-2D [65]	613MCI + 360CN	61.81	92.82	14.65	58.55	74.57
Biceph-Net [34]	613MCI + 360CN	62.63	90.17	18.52	54.35	74.82
CDFA [22]	613MCI + 360CN	60.98	46.74	82.64	67.82	59.11
ResNet-18	613MCI + 360CN	64.92	71.74	54.55	64.09	71.16
ResNet-50	613MCI + 360CN	61.31	99.46	3.31	56.21	75.62
ResNet-101	613MCI + 360CN	63.28	91.85	19.83	59.95	75.11
MRN	613MCI + 360CN	73.77	89.13	50.41	73.14	80.39

^aMeans just as a reference since the selected experimental data and data preprocessing processes in these methods are different.

methods with the same inputs. Meanwhile, our proposed approach produces the highest classification ACC (73.77%), which is 8.85% higher than the highest accuracy using the same experimental data yielded by ResNet-18. The MRN, which is a region-level method, is generally superior to subject-level methods. A possible reason for this is that region-level representations with multi-relation reasoning could learn more discriminative local features and discard invalid features. The results report that the diagnostic accuracy of MCI is signally lower than that of the other states, indicating that the challenge lies in identifying adjacent disease states. Because MCI is an intermediate stage between CN and AD, which does not significantly affect the daily life of patients, it is difficult to diagnose MCI.

AD vs. MCI vs. CN: In the challenging multi-class diagnosis task, the proposed MRN is further compared with several SOTA studies, as well as classification methods using the same sMRI data, with the results shown in Table 5. The differences in pathological brain changes among the three categories is very subtle. Early-stage MCI patients with low lesions are more like CN subjects, whereas MCI patients in later stages are more similar to early-stage AD patients with more extensive and severe abnormalities, making the multi-class diagnosis problem challenging.

As shown in Table 5, our MRN has dominant performance compared to competing methods with the same experimental data or existing methods [32,68] using different sMRI scans. For example, MRN achieves an ACC of 63.23% and an F1 of 60.23%, which are 9.19% and 5.37% higher than those of the subject-level CDFA method [22], respectively. Furthermore, the region-level MRN method clearly shows advantages over subject-level methods. For instance, MRN outperforms ResNet-18 with gains of 3.34%, 1.56% and 2.42% regarding ACC, AUC and F1, respectively.

Specifically, MRN achieves a superior improvement in SEN, meaning that it has a lower omission diagnostic rate for multi-class diagnosis. This suggests that the proposed framework is more sensitive to changes in the brain anatomy associated with the disease. Further analysis is performed using the confusion matrix for multi-class classification, as provided in Fig. 5. The correct prediction for each label is displayed on the diagonal of the matrix. We can observe that the most difficult challenge is to distinguish CN from MCI, in which for the CN label, MRN likely misclassifies it as an MCI label. Because the brains of older subjects already show signs of neurodegeneration associated with aging, which explains the lower accuracy of the CN class. However, the high sensitivity in distinguishing between CN and MCI indicates fewer false negative results, which helps detect patients with MCI and AD at an early stage. Overall, the confusion matrix reflects that MRN can generate clear boundaries between labels, especially CN vs. AD. In conclusion, the experimental results indicate that our proposed approach employing multi-relation reasoning in brain regions to extract semantic and spatial correlations achieves competitive performance, irrespective of two-class classification tasks or the multi-class classification task.

4.3.2. Comparison of computational complexity

In this section, the computational complexities are listed in Table 6. To compare the space and time costs, three metrics are selected: total number of parameters in millions (Params), the model size on disk in megabytes (Size), and floating point of operations (FLOPs). To facilitate comparison, models trained on the AD vs. CN classification task by these methods are adopted. ResNet-18 occupies 385 MB, CDFA [22] occupies 345 MB, while MRN only takes up 26.50 MB. We can observe that our framework occupies

Table 5
Performance comparison with SOTA methods for AD vs. MCI vs. CN classification.

Method	Subjects	AD vs. MCI vs. CN classification (%)				
		ACC	SEN	SPE	AUC	F1
DRN [32] ^a	188AD + 243MCI + 229CN	56.80	-	-	-	-
JMLRC [68] ^a	79AD + 190MCI + 143CN	58.40	-	-	-	57.60
Extended-2D [65]	345AD + 613MCI + 360CN	52.14	37.41	68.18	60.85	33.30
Biceph-Net [34]	345AD + 613MCI + 360CN	52.09	36.06	67.40	64.07	28.10
CDFA [22]	345AD + 613MCI + 360CN	54.04	60.23	75.98	72.61	54.86
ResNet-18	345AD + 613MCI + 360CN	59.89	56.78	76.03	73.54	57.81
ResNet-50	345AD + 613MCI + 360CN	56.55	47.67	73.10	71.16	49.78
ResNet-101	345AD + 613MCI + 360CN	58.50	56.33	75.73	69.66	58.38
MRN	345AD + 613MCI + 360CN	63.23	59.34	78.13	75.10	60.23

^aMeans just as a reference since the selected experimental data and data preprocessing processes in these methods are different.

Table 6
Comparison results in terms of Params, Size and FLOPs.

Model	Params (M)	Size (MB)	FLOPs (G)
Extended-2D [65]	1.36	5.27	0.42
Biceph-Net [34]	14.99	58.00	16.84
ResNet-18	128.45	385.00	178.20
ResNet-50	183.88	552.00	240.61
ResNet-101	332.83	999.00	375.56
CDFA [22]	89.75	345.00	99.11
MRN	8.76	26.50	97.77

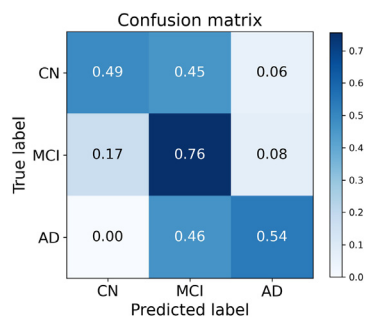


Fig. 5. Confusion matrix of MRN for multi-class diagnosis.

significantly less space on the disk. In addition, the proposed method outperforms by 3.43% over ResNet-18, which is approximately twice that of the complex (178.20G FLOPs). Moreover, the proposed method is significantly more space efficient than ResNet-18 in terms of Params (fourteen times fewer parameters). MRN yields competitive performance in AD diagnosis, while is superior in terms of computational complexity. Our proposed method reduces the time and cost of AD diagnosis and has the potential to be a useful clinical tool for the early diagnosis of AD.

4.4. Ablation study

4.4.1. Ablation study for region representation

In the proposed network shown in Fig. 3, the DC module is employed to learn the informative representation of disease-affected brain regions. To investigate the effectiveness of the DC module, we further conduct a group of experiments by using ResNet-18, the standard convolution module instead of dilated convolution, the DC module, and the DC module replacing IN with batch normalization (BN), respectively, and denote these four variants as 'ResNet', 'Conv', 'DC (IN)' and 'DC (BN)'. Note that the region representations are concatenated and directly fed to the classifier without the LR module for disease diagnosis to verify the effectiveness of our proposed DC module. The experimental results are given in Fig. 6.

Looking at Fig. 6, it is apparent that the proposed DC module obtains better results compared with the other three methods in terms of all evaluation metrics for the two-class diagnosis. In addition, the superiority of 'DC (IN)' over 'Conv', 'ResNet' and 'DC (BN)' is particularly obvious in multi-class classification. For example, 'DC (IN)' obtains favorable results with an ACC of 60.17% and an F1 of 57.54%, which are 1.40% and 0.73% higher than 'Conv', 5.85% and 10.92% higher than 'DC (BN)', and 5.57% and 14.25% than 'ResNet'. The reason could be that the DC module with different dilation rates learns more informative representations of the discriminative regions. As the brain regions are relatively small and varied in size, it is difficult to extract rich region features through traditional CNN, such as 'Conv' and 'ResNet'. Learning rich region representations using dilations in the convolution layers without additional computational overhead is crucial for AD diagnosis. Moreover, different from the BN, IN is computed only across the feature spatial dimensions, but again independently for each channel and sample. Therefore, 'DC (IN)' can not only accelerate model convergence but also maintain the independence between each sMRI scan potentially leading to higher accuracy.

4.4.2. Ablation study for multi-relation reasoning

In the proposed MRN, multi-relation reasoning based on GCN is employed on brain connectivity graphs (semantic and spatial graphs) to learn spatial correlations and topological information between disease-affected brain regions. To further investigate the effectiveness of each inter-region relation for AD diagnosis, we perform experiments by comparing MRN with its variants with a single correlation, denoted as 'Semantic' and 'Spatial', respectively. The results are reported in Fig. 7.

We notice that our proposed MRN that learns spatial correlations and potential interactions between discriminative brain regions obtains the best performance in most cases, especially in the AD vs. CN diagnosis task. For instance, MRN method obtains competing results (92.57%, 97.64% and 87.38% for ACC, AUC and F1, respectively) for the AD vs. CN classification. Additionally, in the MCI vs. CN diagnosis, the ACC (73.77%) and F1 (80.39%) achieved by our proposed method are also much better. These empirical results support our observation that exploiting both the location information and semantic correlations of discriminative brain regions in MRI scans can assist in AD-related disease diagnosis. Moreover, 'Semantic' and 'Spatial' generally yield worse performance, compared to MRN. This clearly indicates that methods focusing on only one type of relationship cannot learn reasonable features to represent structural changes and connectivity representations of the brain, while there may be interactional relations between atrophied brain regions.

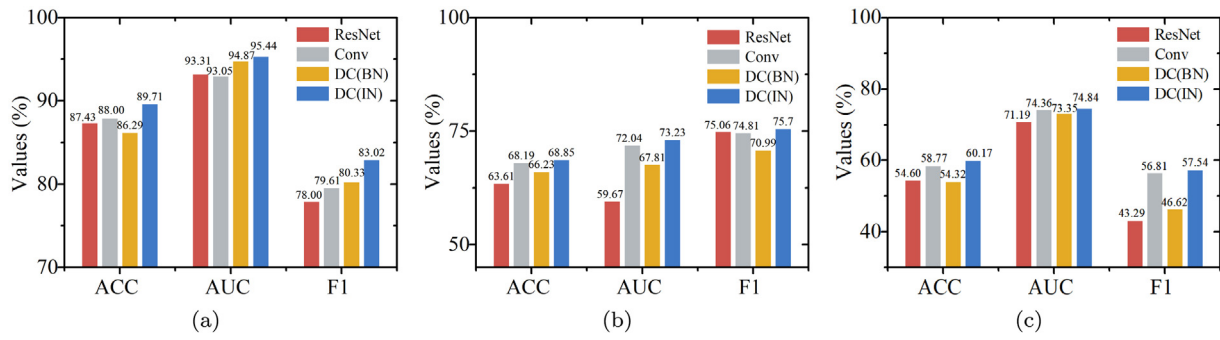


Fig. 6. Performance of methods using different region representations. (a) AD vs. CN. (b) MCI vs. CN. (c) AD vs. MCI vs. CN.

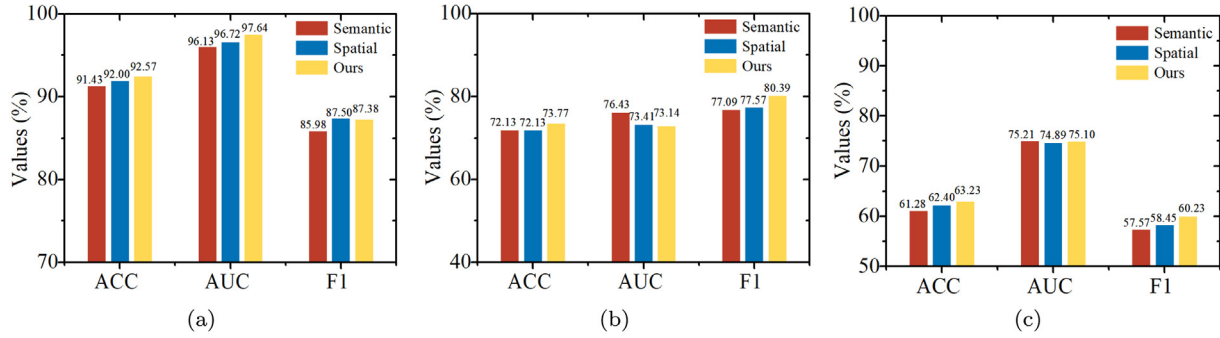


Fig. 7. Performance of methods using different relation reasoning. (a) AD vs. CN. (b) MCI vs. CN. (c) AD vs. MCI vs. CN.

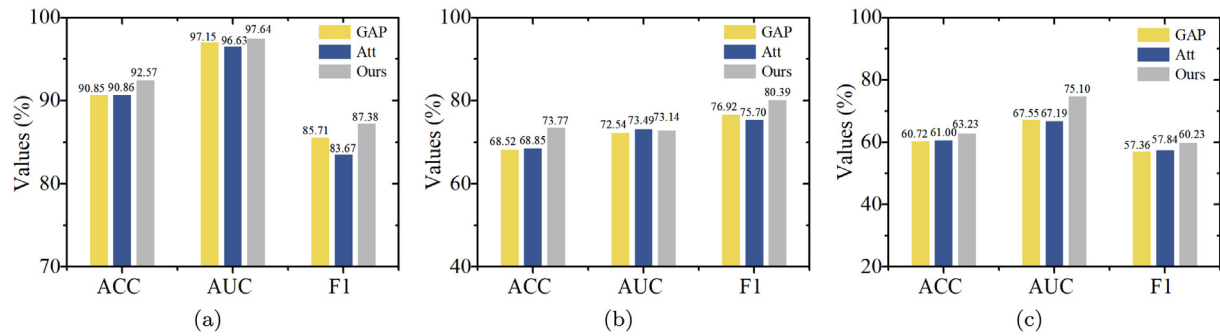


Fig. 8. Performance of methods using different subject-level representations. (a) AD vs. CN. (b) MCI vs. CN. (c) AD vs. MCI vs. CN.

4.4.3. Ablation study for subject-level representation

To investigate the effectiveness of global reasoning using GRU, we conduct experiments to compare MRN with different variants that use widely adopted aggregation methods. The variants utilizing global average pooling and attention mechanism to learn the subject-level representation are denoted as ‘GAP’ and ‘Att’, respectively. The experimental results are shown in Fig. 8. We can observe that MRN outperforms the other two variants in the three classification tasks in terms of most evaluation metrics. For instance, the proposed MRN has dominant performance among comparison methods in AD vs. MCI vs. CN classification, with an accuracy of 63.23% and an AUC of 75.10%, which are 2.51% and 7.55% higher than ‘GAP’, and 2.23% and 7.91% higher than ‘Att’. For the challenging task, MCI vs. CN, as can be seen from Fig. 8, global reasoning using GRU shows advantages over the other two aggregation methods, for example, it outperforms ‘GAP’ with gains of 5.25%, 0.60% and 3.47% regarding ACC, AUC and F1. A reasonable explanation is that using GRU to learn the subject-level representation can efficiently consider both the local region and global correlations, while ‘GAP’ lacks attentively selecting the useful information and ‘Att’ has no focus on global correlations.

5. Discussion

5.1. Results using different validation strategies

To further evaluate the robustness and generalization ability of the proposed MRN model, we perform additional groups of experiments with two validation strategies.

In the first group of experiments, we adopt a 5-fold cross-validation strategy to comprehensively evaluate the validity and stability of our proposed and compared methods. Specifically, the whole dataset is randomly partitioned into five subsets (with approximately equal sizes), and the scans within one subset are selected as the test data each time, while the rest four subsets are used to train the models. The experimental results of Extended-2D [65], Biceph-Net [34], CDFA [22], ResNet18, and MRN are shown in Fig. 9. We can find that our MRN method achieves a better performance in both two-class and multi-class diagnosis tasks in most cases. For example, in the AD vs. CN classification, the mean ACC, AUC and F1 values achieved by MRN are 91.89%, 95.08% and 89.50%, respectively, which are much better than those of ResNet-18 (ACC = 90.01%, AUC = 94.68% and F1

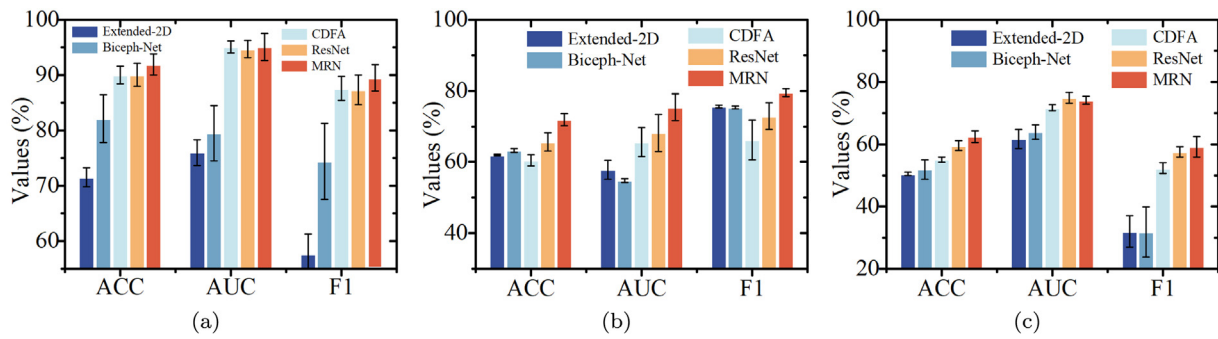


Fig. 9. Average classification results of the 5-fold cross-validation. (Error bars show standard deviation.) (a) AD vs. CN. (b) MCI vs. CN. (c) AD vs. MCI vs. CN.

Table 7

The experimental results when ADNI-2 is the testing set.

Method	AD vs. CN (%)			MCI vs. CN (%)			AD vs. MCI vs. CN (%)		
	ACC	AUC	F1	ACC	AUC	F1	ACC	AUC	F1
Extended-2D [65]	73.28	72.99	45.94	53.47	46.84	69.38	44.81	53.94	23.16
Biceph-Net [34]	82.70	78.53	70.59	56.41	48.24	70.23	44.46	58.35	24.35
CDFA [22]	90.60	93.57	83.48	57.99	62.30	71.16	50.68	70.94	43.63
ResNet-18	88.46	91.19	80.00	58.43	57.81	68.56	51.51	69.33	51.54
MRN	91.10	94.51	85.16	60.31	63.47	65.58	52.61	70.24	49.84

Table 8

Influence of using different hemispheres for AD-related classification tasks.

Method	AD vs. CN classification (%)					MCI vs. CN classification (%)					AD vs. MCI vs. CN classification (%)				
	ACC	SEN	SPE	AUC	F1	ACC	SEN	SPE	AUC	F1	ACC	SEN	SPE	AUC	F1
Left	91.43	81.48	95.87	94.78	85.44	68.20	82.07	47.11	71.85	75.69	62.12	58.16	76.51	76.70	59.07
Right	90.29	77.78	95.87	95.62	83.17	66.56	85.33	38.02	68.94	75.48	60.45	50.53	74.74	71.04	52.55
Left-Right	92.57	83.33	96.69	97.64	87.38	73.77	89.13	50.41	73.14	80.39	63.23	59.34	78.13	75.10	60.23

= 87.29%). In addition, MRN obtains an overall low standard deviation (minimum of 1.09% and a maximum of 3.70%) between the five folds for almost all evaluation metrics.

In the second group of experiments, ADNI-1/GO and ADNI-2 are used as the training and testing sets, respectively, to evaluate the generalization ability of our method. To ensure the independence of the samples, subjects that appeared in ADNI-1 and ADNI-GO are removed from ADNI-2. The final number of scans in the training and testing sets are 2096 and 1093, respectively. The experimental results of the AD vs. CN, MCI vs. CN, and AD vs. MCI vs. CN classification tasks are reported in Table 7.

As shown in Table 7, the proposed MRN method consistently outperforms the compared methods in all performance measures for the AD vs. CN classification. For instance, the F1 value obtained by our method is 85.16%, which is better than the second-best result of 83.48% yielded by the CDFA [22] method. From Table 7, we can also observe that our proposed MRN method generally outperforms competing methods in MCI vs. CN diagnosis on the ADNI-2 testing set. The ACC value achieved by MRN is 60.31%, which is much better than those yielded by Extended-2D [65], Biceph-Net [34], CDFA [22] and ResNet18 methods. It is worth noting that MRI scans from ADNI-2 are scanned using 3T scanners, while scans from ADNI-1 are 1.5T sMRI. Although the MRI scans in the training and test sets may have different signal-to-noise ratios, the proposed MRN can still reliably distinguish patients from cognitively normal people, indicating that our method is robust and generalizable.

5.2. Influence of the number of brain regions

As the proposed method focuses on the regions affected by the disease, avoiding the interference of redundant or noisy information, the number of discriminative brain regions needs to

be set to a reasonable value. We further analyze the influence of the number K of discriminative brain regions on diagnosis performance by shifting it in the set {2, 4, 6, 8, 10, 12}. We report the ACC, F1 and AUC values achieved by MRN with different numbers of paired brain regions in AD-related diagnosis tasks in Fig. 10.

Fig. 10 illustrates that the overall performance increases with the number of brain regions. Eventually, after exceeding a specific value, a further increase in K cannot significantly boost the diagnostic performance. When $K = 6$ in the AD vs. CN classification, the proposed framework achieves the highest ACC, AUC and F1 values of 92.57%, 97.64% and 87.38%, respectively. In particular, for MCI vs. CN classification, our method with $K = 8$ yields satisfactory results with an ACC 73.77% and an F1 80.39%, whereas the overall performance deteriorates rapidly when K exceeds 8. These results indicate the need to set an appropriate K value for multiple AD-related classification tasks. Too many regions can increase the number of network parameters and bring redundant or useless information, resulting in performance degradation, while too few regions cannot significantly represent disease-induced structural changes. Hence, it is reasonable to set K for the AD vs. CN, MCI vs. CN, and AD vs. MCI vs. CN tasks to 6, 8, and 12 respectively.

5.3. Regions of disease progression

For AD diagnosis, sMRI scans generally reveals atrophy of the cerebral cortex during the progression of AD. In this paper, the 12 most discriminative regions are identified through correlation analysis between categories as shown in Fig. 11. Significant brain regions including the hippocampus, amygdala, parahippocampal gyrus, middle temporal gyrus, and inferior temporal gyrus are signed at full views on sMRI scans. This finding is consistent

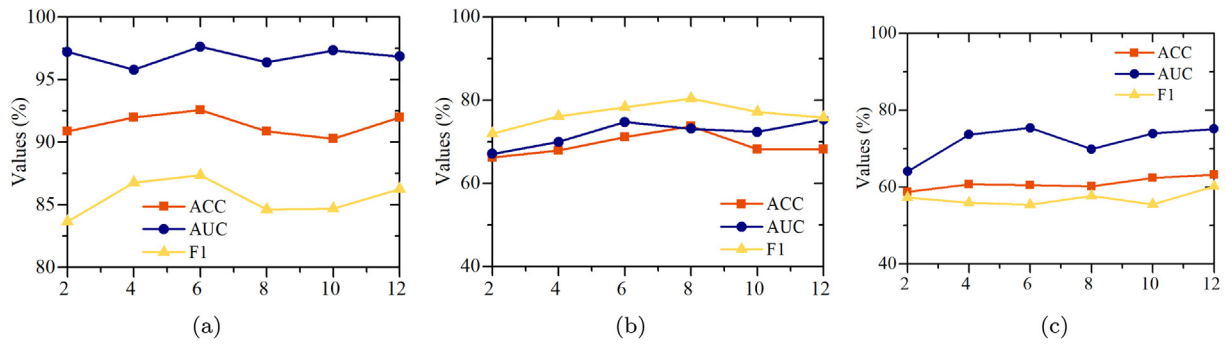


Fig. 10. Influence of the number of brain regions on performance in AD-related diagnosis tasks. (a) AD vs. CN. (b) MCI vs. CN. (c) AD vs. MCI vs. CN.

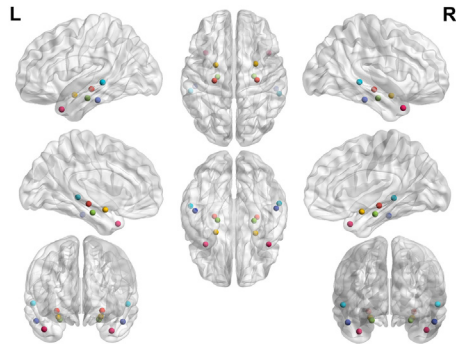


Fig. 11. Identified disease-related brain regions, where letter L stands for the left hemisphere and letter R stands for the right hemisphere.

with those of previous sMRI [24,25] and biochemical studies [69]. Specifically, the hippocampus, one of the brain regions most affected by AD, is responsible for storing and retrieving memory. Brain atrophy in the hippocampus caused by AD has been biologically confirmed [70]. The amygdala plays an important role in regulating and remembering emotions [71] that are also associated with AD. Furthermore, the middle temporal gyrus and inferior temporal gyrus are largely responsible for verbal fluency, semantic memory processing and visual perception, which are cognitive functions affected early in the onset of AD [72]. Therefore, our method employs brain structure analysis using graph theory to extract semantic and topological information from sMRI scans, which can help detect critical changes in brain regions and thus effectively assist in distinguishing AD, MCI, and CN.

5.4. Visualization of semantic and spatial relations

In this section, we present a visualization of the correlation matrices \mathcal{E}_{sem} and \mathcal{E}_{spa} , respectively, to illustrate the learned semantic and spatial relations. The results are shown in Fig. 12, and the full names of the discriminative brain regions are provided in Table 2. As shown in Fig. 12(a), the color in the semantic correlation matrix indicates the strength of the semantic relationship between discriminative brain regions. We find that the higher value appears in 'rMTG' and 'lITG' in the row of 'lMTG', which means that 'rMTG' and 'lITG' are most relevant for 'lMTG' in semantic relation of brain regions for AD diagnosis. Additionally, 'lAMYG', 'lMTG' and 'rTPOmid' have a high relevance score with other discriminative brain regions. The colors in the spatial correlation matrix show different spatial relations between the brain regions. It can be seen from Fig. 12(b), the spatial relations between the two brain regions are symmetric and bidirectional. In general, from the observation of the learned semantic and spatial relations, we can believe that MRN has the capacity to

capture the spatial correlations and potential interactions of discriminative brain regions, which provides valuable information for AD diagnosis.

5.5. Comparison of left and right brain regions

To further investigate the influence of different hemispheres on AD diagnostic performance, two variants of our method (i.e., 'Left' and 'Right') are compared, which only consider left and right brain regions respectively. The experimental results are reported in Table 8.

We can observe that the performance based on left brain regions is doing better than right ones in terms of most evaluation metrics for the three classification tasks. Specifically, the method using left brain regions outperforms the right one with gains of 1.64%, 9.09%, 2.91% and 0.21% regarding ACC, SPE, AUC and F1 for MCI vs. CN classification. And 'Left' has better performance for the multi-class diagnosis task, with an accuracy of 62.12% and a metric F1 of 59.07%, which are 1.67% and 6.52% higher than 'Right'. These results imply that disease-related abnormalities in sMRI scans may develop in an asymmetrical manner, with the left discriminative regions appearing to be more susceptible to AD or MCI than the right ones. Our results concur with previous publications [73,74], which indicate that the left hemisphere appears to have slight preferential atrophy compared to the right in sMRI scans. Furthermore, the best overall performance is achieved by using both the left and right hemispheres, which indicates that our method considering multi-relation reasoning in pairs of left brain and right brain jointly is effective and reasonable.

6. Conclusion

In this study, we propose a novel method named MRN to boost the performance of sMRI-based AD diagnosis and assist in exploring potential imaging biomarkers. Specifically, disease-related regions are identified through group difference analysis, upon which semantic and spatial graphs are constructed. Then, a local reasoning module is designed to effectively learn not only pathological changes in disease-affected brain regions but also their potential associations and interactions, generating region-level representations. Furthermore, global reasoning is performed on region-level representations to select discriminant information and obtain subject-level representations for the final classification. We further investigate the influence of left and right brain regions on the performance of the AD diagnosis, which implies that the left regions have more obvious disease-induced structural changes than the right ones. Experimental results on ADNI demonstrate that MRN outperforms several state-of-the-art approaches in multiple AD classification tasks and that analyzing disease-related brain regions using graph theory can provide critical information for AD diagnosis.

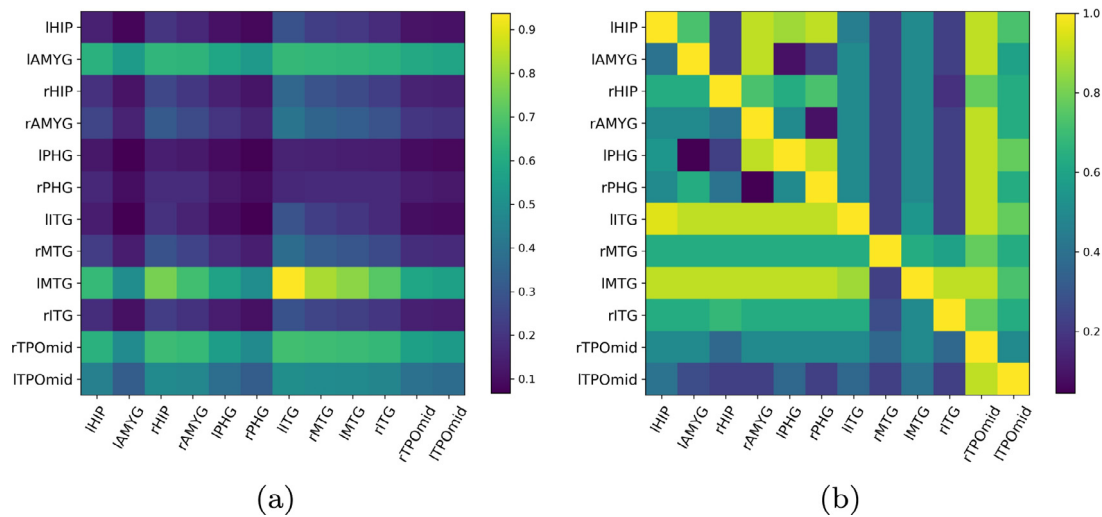


Fig. 12. Visualization of the learned semantic and spatial relations. (a) Semantic correlation matrix. (b) Spatial correlation matrix.

CRedit authorship contribution statement

Jin Zhang: Methodology, Writing – original draft, Investigation, Software. **Xiaohai He:** Supervision, Project administration, Resources, Formal analysis. **Linbo Qing:** Conceptualization, Formal analysis, Supervision. **Xiang Chen:** Writing – review & editing. **Yan Liu:** Visualization, Validation. **Honggang Chen:** Validation, Investigation.

Declaration of competing interest

The authors declare that they have no known competing financial interests or personal relationships that could have appeared to influence the work reported in this paper.

Data availability

Data will be made available on request.

Acknowledgments

The research in our paper is sponsored by Chengdu Major Technology Application Demonstration Project, China (2019-YF09-00120-SN) and the Sichuan Science and Technology Program, China (No. 2021YFS0239). The authors thank the ADNI investigators for providing access to the data. Data used in the preparation of this article are obtained from the Alzheimer’s Disease Neuroimaging Initiative (ADNI) database. For more information about ADNI, see www.adni-info.org.

References

[1] S. Tiwari, V. Atluri, A. Kaushik, A. Yndart, M. Nair, Alzheimer’s disease: pathogenesis, diagnostics, and therapeutics, *Int. J. Nanomedicine* 14 (2019) 5541.
 [2] L. Zhan, J. Zhou, Y. Wang, Y. Jin, N. Jahanshad, G. Prasad, T.M. Nir, C.D. Leonardo, J. Ye, P.M. Thompson, et al., Comparison of nine tractography algorithms for detecting abnormal structural brain networks in Alzheimer’s disease, *Front. Aging Neurosci.* 7 (2015) 48.
 [3] X. Zhu, H.-I. Suk, Y. Zhu, K.-H. Thung, G. Wu, D. Shen, Multi-view classification for identification of Alzheimer’s disease, in: *International Workshop on Machine Learning in Medical Imaging*, Springer, 2015, pp. 255–262.
 [4] W. Jagust, Vulnerable neural systems and the borderland of brain aging and neurodegeneration, *Neuron* 77 (2) (2013) 219–234.
 [5] N. Habib, C. McCabe, S. Medina, M. Varshavsky, D. Kitsberg, R. Dvir-Szternfeld, G. Green, D. Dionne, L. Nguyen, J.L. Marshall, et al., Disease-associated astrocytes in Alzheimer’s disease and aging, *Nature Neurosci.* 23 (6) (2020) 701–706.

[6] Z. Longhe, Alzheimer’s disease facts and figures, *Alzheimer’s Dement.* 16 (2020) 391–460.
 [7] J. Wen, E. Thibau-Sutre, M. Diaz-Melo, J. Samper-González, A. Routier, S. Bottani, D. Dormont, S. Durrleman, N. Burgos, O. Colliot, et al., Convolutional neural networks for classification of Alzheimer’s disease: Overview and reproducibility evaluation, *Med. Image Anal.* 63 (2020) 101694.
 [8] M. Liu, F. Li, H. Yan, K. Wang, Y. Ma, L. Shen, M. Xu, A.D.N. Initiative, et al., A multi-model deep convolutional neural network for automatic hippocampus segmentation and classification in Alzheimer’s disease, *Neuroimage* 208 (2020) 116459.
 [9] T. Abuhmed, S. El-Sappagh, J.M. Alonso, Robust hybrid deep learning models for Alzheimer’s progression detection, *Knowl.-Based Syst.* 213 (2021) 106688.
 [10] X. Pan, T.-L. Phan, M. Adel, C. Fossati, T. Gaidon, J. Wojak, E. Guedj, Multi-view separable pyramid network for AD prediction at MCI stage by 18F-FDG brain PET imaging, *IEEE Trans. Med. Imaging* 40 (1) (2020) 81–92.
 [11] R. Hu, Z. Peng, X. Zhu, J. Gan, Y. Zhu, J. Ma, G. Wu, Multi-band brain network analysis for functional neuroimaging biomarker identification, *IEEE Trans. Med. Imaging* 40 (12) (2021) 3843–3855.
 [12] A.M. Alvi, S. Siuly, H. Wang, K. Wang, F. Whittaker, A deep learning based framework for diagnosis of mild cognitive impairment, *Knowl.-Based Syst.* 248 (2022) 108815.
 [13] X. Chen, T. Wang, H. Lai, X. Zhang, Q. Feng, M. Huang, Structure-constrained combination-based nonlinear association analysis between incomplete multimodal imaging and genetic data for biomarker detection of neurodegenerative diseases, *Med. Image Anal.* 78 (2022) 102419.
 [14] B. Lei, Y. Zhang, D. Liu, Y. Xu, G. Yue, J. Cao, H. Hu, S. Yu, P. Yang, T. Wang, et al., Longitudinal study of early mild cognitive impairment via similarity-constrained group learning and self-attention based SBI-LSTM, *Knowl.-Based Syst.* (2022) 109466.
 [15] G.B. Frisoni, N.C. Fox, C.R. Jack, P. Scheltens, P.M. Thompson, The clinical use of structural MRI in Alzheimer disease, *Nat. Rev. Neurol.* 6 (2) (2010) 67–77.
 [16] C. Salvatore, A. Cerasa, P. Battista, M.C. Gilardi, A. Quattrone, I. Castiglioni, Magnetic resonance imaging biomarkers for the early diagnosis of Alzheimer’s disease: a machine learning approach, *Front. Neurosci.* 9 (2015) 307.
 [17] P. Cao, X. Liu, J. Yang, D. Zhao, M. Huang, J. Zhang, O. Zaiane, Nonlinearity-aware based dimensionality reduction and over-sampling for AD/MCI classification from MRI measures, *Comput. Biol. Med.* 91 (2017) 21–37.
 [18] K. Bäckström, M. Nazari, I.Y.-H. Gu, A.S. Jakola, An efficient 3D deep convolutional network for Alzheimer’s disease diagnosis using MR images, in: *2018 IEEE 15th International Symposium on Biomedical Imaging (ISBI 2018)*, IEEE, 2018, pp. 149–153.
 [19] M. Liu, J. Zhang, D. Nie, P.-T. Yap, D. Shen, Anatomical landmark based deep feature representation for MR images in brain disease diagnosis, *IEEE J. Biomed. Health Inf.* 22 (5) (2018) 1476–1485.
 [20] C. Lian, M. Liu, L. Wang, D. Shen, End-to-end dementia status prediction from brain MRI using multi-task weakly-supervised attention network, in: *International Conference on Medical Image Computing and Computer-Assisted Intervention*, Springer, 2019, pp. 158–167.
 [21] J.E. Arco, J. Ramirez, J.M. Górriz, M. Ruz, A.D.N. Initiative, et al., Data fusion based on searchlight analysis for the prediction of Alzheimer’s disease, *Expert Syst. Appl.* 185 (2021) 115549.

- [22] S. Liu, C. Yadav, C. Fernandez-Granda, N. Razavian, On the design of convolutional neural networks for automatic detection of Alzheimer's disease, in: *ML4H@NeurIPS*, 2019.
- [23] S. Spasov, L. Passamonti, A. Duggento, P. Lio, N. Toschi, A.D.N. Initiative, et al., A parameter-efficient deep learning approach to predict conversion from mild cognitive impairment to Alzheimer's disease, *Neuroimage* 189 (2019) 276–287.
- [24] C. Lian, M. Liu, J. Zhang, D. Shen, Hierarchical fully convolutional network for joint atrophy localization and Alzheimer's disease diagnosis using structural MRI, *IEEE Trans. Pattern Anal. Mach. Intell.* 42 (4) (2018) 880–893.
- [25] W. Zhu, L. Sun, J. Huang, L. Han, D. Zhang, Dual attention multi-instance deep learning for Alzheimer's disease diagnosis with structural MRI, *IEEE Trans. Med. Imaging* 40 (9) (2021) 2354–2366.
- [26] K. Hett, V.-T. Ta, J.V. Manjón, P. Coupé, A.D.N. Initiative, et al., Adaptive fusion of texture-based grading for Alzheimer's disease classification, *Comput. Med. Imaging Graph.* 70 (2018) 8–16.
- [27] M. Plocharski, L.R. Østergaard, A.D.N. Initiative, et al., Extraction of sulcal medial surface and classification of Alzheimer's disease using sulcal features, *Comput. Methods Programs Biomed.* 133 (2016) 35–44.
- [28] S. Klöppel, C.M. Stonnington, C. Chu, B. Draganski, R.I. Scahill, J.D. Rohrer, N.C. Fox, C.R. Jack Jr., J. Ashburner, R.S. Frackowiak, Automatic classification of MR scans in Alzheimer's disease, *Brain* 131 (3) (2008) 681–689.
- [29] L. Wang, F. Beg, T. Ratnanather, C. Ceritoglu, L. Younes, J.C. Morris, J.G. Csernansky, M.I. Miller, Large deformation diffeomorphism and momentum based hippocampal shape discrimination in dementia of the Alzheimer type, *IEEE Trans. Med. Imaging* 26 (4) (2007) 462–470.
- [30] L. Sørensen, C. Igel, N. Liv Hansen, M. Osler, M. Lauritzen, E. Rostrup, M. Nielsen, Alzheimer's Disease Neuroimaging Initiative, the Australian Imaging Biomarkers, Lifestyle Flagship Study of Ageing, Early detection of Alzheimer's disease using M RI hippocampal texture, *Human Brain Mapp.* 37 (3) (2016) 1148–1161.
- [31] O.B. Ahmed, M. Mizotin, J. Benois-Pineau, M. Allard, G. Catheline, C.B. Amar, A.D.N. Initiative, et al., Alzheimer's disease diagnosis on structural MR images using circular harmonic functions descriptors on hippocampus and posterior cingulate cortex, *Comput. Med. Imaging Graph.* 44 (2015) 13–25.
- [32] A.A. Valliani, A. Soni, Deep residual nets for improved Alzheimer's diagnosis, in: *Proceedings of the 8th ACM International Conference on Bioinformatics, Computational Biology, and Health Informatics*, 2017.
- [33] J. Islam, Y. Zhang, Brain MRI analysis for Alzheimer's disease diagnosis using an ensemble system of deep convolutional neural networks, *Brain Inform.* 5 (2) (2018) 1–14.
- [34] A.H. Rashid, A. Gupta, J. Gupta, M. Tanveer, Biceph-Net: A robust and lightweight framework for the diagnosis of Alzheimer's disease using 2D-MRI scans and deep similarity learning, *IEEE J. Biomed. Health Inf.* (2022).
- [35] J. Zhang, M. Liu, L. An, Y. Gao, D. Shen, Alzheimer's disease diagnosis using landmark-based features from longitudinal structural MR images, *IEEE J. Biomed. Health Inf.* 21 (6) (2017) 1607–1616.
- [36] C. Lian, M. Liu, Y. Pan, D. Shen, Attention-guided hybrid network for dementia diagnosis with structural MR images, *IEEE Trans. Cybern.* (2020).
- [37] S. Qiu, P.S. Joshi, M.I. Miller, C. Xue, X. Zhou, C. Karjadi, G.H. Chang, A.S. Joshi, B. Dwyer, S. Zhu, et al., Development and validation of an interpretable deep learning framework for Alzheimer's disease classification, *Brain* 143 (6) (2020) 1920–1933.
- [38] M. Liu, J. Zhang, E. Adeli, D. Shen, Landmark-based deep multi-instance learning for brain disease diagnosis, *Med. Image Anal.* 43 (2018) 157–168.
- [39] M. Wang, D. Zhang, D. Shen, M. Liu, Multi-task exclusive relationship learning for Alzheimer's disease progression prediction with longitudinal data, *Med. Image Anal.* 53 (2019) 111–122.
- [40] V. Gonuguntla, E. Yang, Y. Guan, B.-B. Koo, J.-H. Kim, Brain signatures based on structural MRI: Classification for MCI, PMCI, and AD, *Human Brain Mapp.* (2022).
- [41] S. Korolev, A. Safiullin, M. Belyaev, Y. Dodonova, Residual and plain convolutional neural networks for 3D brain MRI classification, in: *2017 IEEE 14th International Symposium on Biomedical Imaging (ISBI 2017)*, IEEE, 2017, pp. 835–838.
- [42] X. Zhang, L. Han, W. Zhu, L. Sun, D. Zhang, An explainable 3D residual self-attention deep neural network for joint atrophy localization and Alzheimer's disease diagnosis using structural MRI, *IEEE J. Biomed. Health Inf.* (2021).
- [43] Z. Liu, H. Lu, X. Pan, M. Xu, R. Lan, X. Luo, Diagnosis of Alzheimer's disease via an attention-based multi-scale convolutional neural network, *Knowl.-Based Syst.* 238 (2022) 107942.
- [44] S. Parisot, S.I. Ktena, E. Ferrante, M. Lee, R. Guerrero, B. Glocker, D. Rueckert, Disease prediction using graph convolutional networks: application to autism spectrum disorder and Alzheimer's disease, *Med. Image Anal.* 48 (2018) 117–130.
- [45] Y. Zhu, J. Ma, C. Yuan, X. Zhu, Interpretable learning based dynamic graph convolutional networks for Alzheimer's disease analysis, *Inf. Fusion* 77 (2022) 53–61.
- [46] H. Zhou, L. He, Y. Zhang, L. Shen, B. Chen, Interpretable graph convolutional network of multi-modality brain imaging for Alzheimer's disease diagnosis, in: *2022 IEEE 19th International Symposium on Biomedical Imaging (ISBI)*, IEEE, 2022, pp. 1–5.
- [47] D. Jin, J. Xu, K. Zhao, F. Hu, Z. Yang, B. Liu, T. Jiang, Y. Liu, Attention-based 3D convolutional network for Alzheimer's disease diagnosis and biomarkers exploration, in: *2019 IEEE 16th International Symposium on Biomedical Imaging (ISBI 2019)*, 2019, pp. 1047–1051.
- [48] C.R. Jack Jr., M.A. Bernstein, N.C. Fox, P. Thompson, G. Alexander, D. Harvey, B. Borowski, P.J. Britson, J. L. Whitwell, C. Ward, et al., The Alzheimer's disease neuroimaging initiative (ADNI): MRI methods, *J. Magn. Reson. Imaging: Off. J. Int. Soc. Magn. Reson. Med.* 27 (4) (2008) 685–691.
- [49] A. Payan, G. Montana, Predicting Alzheimer's disease: a neuroimaging study with 3D convolutional neural networks, 2015, arXiv preprint arXiv:1502.02506.
- [50] Y.R. Fung, Z. Guan, R. Kumar, J.Y. Wu, M. Fiterau, Alzheimer's disease brain MRI classification: Challenges and insights, 2019, arXiv preprint arXiv:1906.04231.
- [51] A. Routier, N. Burgos, J. Guillon, J. Samper-González, J. Wen, S. Bottani, A. Marcoux, M. Bacci, S. Fontanella, T. Jacquemont, A. Wild, P. Gori, A. Guyot, P. Lu, M. Diaz, E. Thibeau-Sutre, T. Moreau, M. Teichmann, M. Habert, S. Durrleman, O. Colliot, Clinica: an open source software platform for reproducible clinical neuroscience studies, 2019.
- [52] B. Fischl, *FreeSurfer*, *NeuroImage* 62 (2012) 774–781.
- [53] E.T. Rolls, C.-C. Huang, C.-P. Lin, J. Feng, M. Joliot, Automated anatomical labelling atlas 3, *Neuroimage* 206 (2020) 116189.
- [54] M.G. Kendall, A new measure of rank correlation, *Biometrika* 30 (1/2) (1938) 81–93.
- [55] Z. Ning, Q. Xiao, Q. Feng, W. Chen, Y. Zhang, Relation-induced multi-modal shared representation learning for Alzheimer's disease diagnosis, *IEEE Trans. Med. Imaging* 40 (2021) 1632–1645.
- [56] J. Ye, J. He, X. Peng, W. Wu, Y. Qiao, Attention-driven dynamic graph convolutional network for multi-label image recognition, in: *European Conference on Computer Vision*, Springer, 2020, pp. 649–665.
- [57] A. Vaswani, N. Shazeer, N. Parmar, J. Uszkoreit, L. Jones, A.N. Gomez, Ł. Kaiser, I. Polosukhin, Attention is all you need, *Adv. Neural Inf. Process. Syst.* 30 (2017).
- [58] K. Li, Y. Zhang, K. Li, Y. Li, Y. Fu, Visual semantic reasoning for image-text matching, in: *Proceedings of the IEEE/CVF International Conference on Computer Vision*, 2019, pp. 4654–4662.
- [59] J. Chung, Ç. Gülçehre, K. Cho, Y. Bengio, Empirical evaluation of gated recurrent neural networks on sequence modeling, 2014, arXiv:1412.3555.
- [60] D.P. Kingma, J. Ba, Adam: A method for stochastic optimization, 2014, arXiv preprint arXiv:1412.6980.
- [61] Y. Zhao, B. Ma, P. Jiang, D. Zeng, X. Wang, S. Li, Prediction of Alzheimer's disease progression with multi-information generative adversarial network, *IEEE J. Biomed. Health Inf.* 25 (3) (2020) 711–719.
- [62] M. Sokolova, G. Lalpalmé, A systematic analysis of performance measures for classification tasks, *Inf. Process. Manage.* 45 (4) (2009) 427–437.
- [63] M. Grandini, E. Bagli, G. Visani, Metrics for multi-class classification: an overview, 2020, arXiv preprint arXiv:2008.05756.
- [64] K. He, X. Zhang, S. Ren, J. Sun, Deep residual learning for image recognition, in: *2016 IEEE Conference on Computer Vision and Pattern Recognition (CVPR)*, 2016, pp. 770–778.
- [65] M. Pereira, I. Fantini, R. Lotufo, L. Rittner, An extended-2D CNN for multiclass Alzheimer's disease diagnosis through structural MRI, in: *Medical Imaging 2020: Computer-Aided Diagnosis*, Vol. 11314, SPIE, 2020, pp. 438–444.
- [66] K.M. Poloni, R.J. Ferrari, Automated detection, selection and classification of hippocampal landmark points for the diagnosis of Alzheimer's disease, *Comput. Methods Programs Biomed.* 214 (2022) 106581.
- [67] K.M. Poloni, I.A.D. de Oliveira, R. Tam, R.J. Ferrari, A.D.N. Initiative, et al., Brain MR image classification for Alzheimer's disease diagnosis using structural hippocampal asymmetrical attributes from directional 3-D log-gabor filter responses, *Neurocomputing* 419 (2021) 126–135.
- [68] L. Brand, K. Nichols, H. Wang, L. Shen, H. Huang, Joint multi-modal longitudinal regression and classification for Alzheimer's disease prediction, *IEEE Trans. Med. Imaging* 39 (6) (2020) 1845.
- [69] A. Du, N. Schuff, D. Amend, M. Laakso, Y. Hsu, W. Jagust, K. Yaffe, J. Kramer, B. Reed, D. Norman, et al., Magnetic resonance imaging of the entorhinal cortex and hippocampus in mild cognitive impairment and Alzheimer's disease, *J. Neurol. Neurosurg. Psychiatry* 71 (4) (2001) 441–447.
- [70] C. Pennanen, M. Kivipelto, S. Tuomainen, P. Hartikainen, T. Hänninen, M.P. Laakso, M. Hallikainen, M. Vanhanen, A. Nissinen, E.-L. Helkala, et al., Hippocampus and entorhinal cortex in mild cognitive impairment and early AD, *Neurobiol. Aging* 25 (3) (2004) 303–310.

- [71] J.P. Aggleton, *The Amygdala: Neurobiological Aspects of Emotion, Memory, and Mental Dysfunction*, Wiley-Liss, 1992.
- [72] A. Convit, J. De Asis, M. De Leon, C. Tarshish, S. De Santi, H. Rusinek, Atrophy of the medial occipitotemporal, inferior, and middle temporal gyri in non-demented elderly predict decline to Alzheimer's disease, *Neurobiol. Aging* 21 (1) (2000) 19–26.
- [73] R.I. Scahill, J.M. Schott, J.M. Stevens, M.N. Rossor, N.C. Fox, Mapping the evolution of regional atrophy in Alzheimer's disease: unbiased analysis of fluid-registered serial MRI, *Proc. Natl. Acad. Sci.* 99 (7) (2002) 4703–4707.
- [74] J.M. Roe, D. Vidal-Piñeiro, Ø. Sørensen, A.M. Brandmaier, S. Düzel, H.A. Gonzalez, R.A. Kievit, E. Knights, S. Kühn, U. Lindenberger, et al., Asymmetric thinning of the cerebral cortex across the adult lifespan is accelerated in Alzheimer's disease, *Nature Commun.* 12 (1) (2021) 1–11.